

Path Entanglement of Continuous-Variable Quantum Microwaves

E. P. Menzel,^{1,2,*} R. Di Candia,³ F. Deppe,^{1,2} P. Eder,^{1,2} L. Zhong,^{1,2} M. Ihmig,⁴
M. Haerberlein,^{1,2} A. Baust,^{1,2} E. Hoffmann,^{1,2} D. Ballester,^{5,3} K. Inomata,⁶
T. Yamamoto,^{7,6} Y. Nakamura,^{8,6} E. Solano,^{3,9} A. Marx,¹ and R. Gross^{1,2}

¹*Walther-Meißner-Institut, Bayerische Akademie der Wissenschaften, D-85748 Garching, Germany*

²*Physik-Department, Technische Universität München, D-85748 Garching, Germany*

³*Departamento de Química Física, Universidad del País Vasco UPV/EHU, 48080 Bilbao, Spain*

⁴*Lehrstuhl für Integrierte Systeme, Technische Universität München, D-80333 München, Germany*

⁵*Department of Physics and Astronomy, University College London, London WC1E 6BT, United Kingdom*

⁶*RIKEN Advanced Science Institute, Wako, Saitama 351-0198, Japan*

⁷*NEC Smart Energy Research Laboratories, Tsukuba, Ibaraki, 305-8501, Japan*

⁸*Research Center for Advanced Science and Technology (RCAST),*

The University of Tokyo, Komaba, Meguro-ku, Tokyo 153-8904, Japan

⁹*IKERBASQUE, Basque Foundation for Science, 48011 Bilbao, Spain*

Path entanglement constitutes an essential resource in quantum information and communication protocols. Here, we demonstrate frequency-degenerate entanglement between continuous-variable quantum microwaves propagating along two spatially separated paths. We combine a squeezed and a vacuum state using a microwave beam splitter. Via correlation measurements, we detect and quantify the path entanglement contained in the beam splitter output state. Our experiments open the avenue to quantum teleportation, quantum communication, or quantum radar with continuous variables at microwave frequencies.

PACS numbers: 03.67.Bg, 03.65.Ud, 42.50.Dv, 85.25.-j

Fascinatingly, quantum mechanics allows for a compound system to have a common description while, at the same time, no individual states can be ascribed to its subsystems¹. The presence of entanglement between spatially separated systems is a necessary condition for what Einstein called “spooky action at a distance”²: the contradiction between quantum mechanics and local realism^{1,3}. Furthermore, entanglement is at the heart of quantum communication and information processing technologies, which promise significant performance gains over classical protocols^{1,4,5}. Consequently, entanglement has been extensively explored in atomic physics and quantum optics⁴⁻⁶. In these investigations, optical frequencies were preferred over microwaves because the higher photon energies facilitate practical applications. However, since the late 1990s, microwave technology has evolved rapidly in both industry and science. For one thing, classical microwave fields have become an indispensable tool in mobile communication. For another, a promising direction towards scalable quantum information processing has appeared with the advent of superconducting microwave quantum circuits⁷⁻⁹. Despite some decoherence issues, these systems provide unprecedented light-matter coupling strengths due to their large effective dipole moments and field enhancement effects^{10,11}. As a consequence, standing-wave fields in transmission line resonators were shown to act as a short-range quantum bus between superconducting qubits^{12,13} and various gates were implemented¹²⁻¹⁶. For microwave quantum communication, however, propagating fields are required. As a first step in this direction, early experiments demonstrated tomography of weak thermal states¹⁷, coherent states¹⁸, and single pho-

tons¹⁹. Next, continuous-variable states generated by Josephson parametric devices were reconstructed²⁰. Very recently, such devices have permitted to investigate two-mode squeezing²¹⁻²³. An important aspect of these experiments is the understanding they provide regarding entanglement. In order to be a resource in quantum communication protocols, it must occur between spatially separated subsystems¹. Furthermore, a strict proof of entanglement requires the entangler and the detector to be based on independent experimental techniques. In this work, we make a significant step beyond previous efforts and demonstrate path entanglement in the microwave regime, respecting both criteria mentioned above. Our experiments follow the spirit of the quantum-optical realization⁶ of the original Einstein-Podolsky-Rosen (EPR) paradox³. As shown in Fig. 1, we combine a vacuum and a squeezed vacuum state in a hybrid ring microwave beam splitter²⁴ acting as an entangling device. Its two output ports hold a continuous-variable state which is frequency-degenerate and entangled with respect to the two propagation paths. Along these paths, the entanglement can be conveniently distributed to two parties requiring it for any suitable quantum communication protocol. In our experiments, we first reconstruct the squeezed *input* state by means of dual-path tomography¹⁸, which assumes knowledge of the beam splitter relations. Next, we reconstruct the moments of the *output* state after the beam splitter by treating the latter as a black box and calibrating against a known state²⁵. In this reference-state method (see Supplementary), we only assume that independent vacuum states are produced in each output path when vacuum is incident at both input ports. From the moments reconstructed in this way, we build

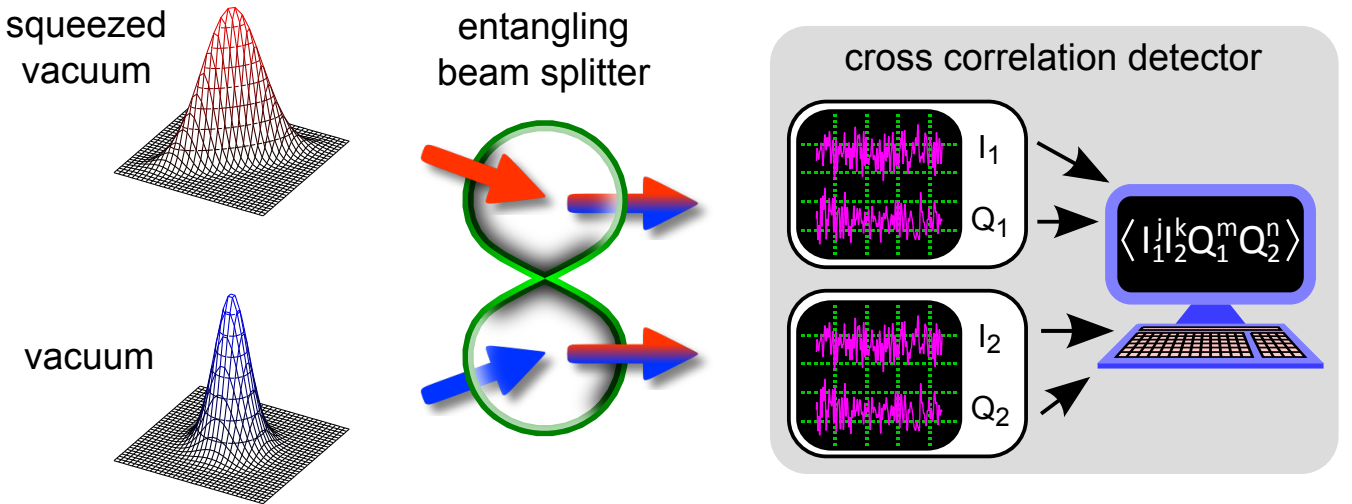


FIG. 1. Layout of the experiment. The microwave beam splitter acts as entangling device (green eight-shaped structure). The blue-and- red arrows denote the path-entangled state. In the cross correlation detector, the oscilloscope symbols denote the noisy amplification, down-conversion, and digitizing of the in-phase ($I_{1,2}$) and quadrature ($Q_{1,2}$) components of the output signals. The computer symbolizes the final numerical data processing, partly done by an FPGA logic.

a witness matrix which proves the existence of path entanglement independently of the detailed nature of our output state²⁶. Since in practice the data shows that our states are Gaussian, we finally quantify the degree of entanglement by means of the negativity²⁷. The result of this analysis agrees with what we expect for our squeezed input state. We note here that for bipartite single-mode Gaussian entanglement, as it is relevant in our case, entanglement implies nonlocality^{1,5}. All in all, our results show that we have realized the main building block for microwave quantum teleportation and communication protocols.

The generation of the input states for the beam splitter is straightforward. The vacuum is realized with a commercial $50\ \Omega$ -termination at 40 mK acting as a broadband black-body emitter¹⁷. The squeezed state is produced using a particular superconducting circuit, the flux-driven Josephson parametric amplifier (JPA)²⁸. In this device two Josephson junctions form a nonlinearity which can be modulated (“pumped”) at gigahertz frequencies to achieve a parametric effect. The JPA box is stabilized to 50 mK. A thermal state emitted by an attenuator, whose temperature can be varied from 50 – 800 mK, can be fed into the JPA. Our cross correlation detector is based on the insight that for microwave signals off-the-shelf high-gain low-noise linear amplifiers are available rather than efficient single photon counters. We connect one amplification path to each output port of the beam splitter. At room temperature we record the in-phase and quadrature components, $I_{1,2}$ and $Q_{1,2}$ of the amplified signals. The averaged moments $\langle I_1^j I_2^k Q_1^m Q_2^n \rangle$ are computed for $j + k + m + n \leq 4$ and $j, k, m, n \in \mathbb{N}_0$ in real time using a field programmable gate array (FPGA) logic. Further details can be found in the Supplementary.

As a first test of our setup, we perform dual-path reconstructions of the Wigner function for known input states. Here, we exploit the fact that the noise contributions of the two amplification paths are independent, while the split signals are correlated¹⁸(see Supplementary). We reconstruct vacuum fluctuations and coherent states (displaced vacuum), both at a frequency $f_0 = 5.637$ GHz. Because of narrow-band filtering, we approximate the vacuum and thermal states as single-mode fields. The results shown in Fig. 2(a) exhibit a very good phase control for the coherent state. In addition, we find a small thermal contribution of 0.097 ± 0.007 photons above the vacuum level which can be due to a small thermal population or other experimental imperfections. In the next step, we generate a squeezed state by pumping the JPA. For a signal gain of 10 dB and a phase of 45° , the reconstructed Wigner function is shown in Fig. 2(b). An analysis of the reconstructed signal moments reveals that, at the input of the beam splitter, the state generated by the JPA is squeezed by 4.9 ± 0.2 dB below the vacuum level and contains 8.72 ± 0.05 photons. Furthermore, the product of the standard deviation of the squeezed quadrature with that of its orthogonal, enlarged one, is 3.45 ± 0.07 times larger than the variance of the ideal vacuum. In other words, we can model the state as one created by an ideal squeezer acting on an effective thermal field with 1.22 ± 0.04 photons. This thermal field contains the combined effects of losses and the small thermal population found in the experimental vacuum. Again, we notice good control of the phase. It is noteworthy to mention that the amount of squeezing quoted above is mainly limited by cable losses and not by the JPA itself.

After characterizing the input fields of the beam splitter, we now turn to its outputs. With the reference-state method, we build an entanglement witness matrix from

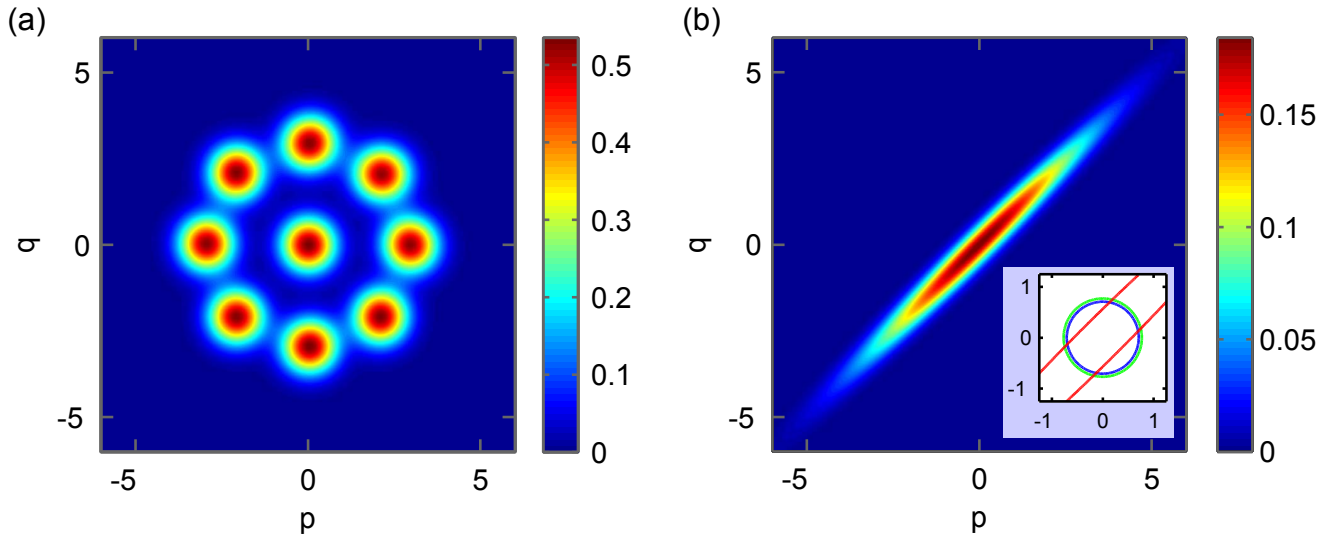


FIG. 2. Dual-path reconstruction of various states incident at the “squeezed state input port” of the beam splitter. p and q are dimensionless variables spanning the phase space. (a) JPA pump off. Reconstruction of the vacuum and of displaced vacuum states (coherent states, 8.80 ± 0.01 photons, eight different phase values). All nine Wigner functions are superposed. (b) JPA pump on. Squeezed state for 10 dB JPA signal gain at 45° . Inset: $1/e$ contours of the ideal vacuum (blue), the experimental vacuum (green) displayed in panel (a), and the squeezed state (red).

the reconstructed moments. Our witness reliably distinguishes between “separable outputs” for the vacuum state and “path entangled outputs” for the squeezed state input. Next, we analyze the third and fourth order cumulants and find them to be small for JPA signal gains up to 10 dB. Since this is a strong indication for Gaussian states, we explore the path entanglement generated in our setup quantitatively via the negativity \mathcal{N}_{out} . For positive values, \mathcal{N}_{out} describes the degree of entanglement produced between the beam splitter output paths (see Supplementary). In the limit of low JPA signal gain, Fig. 3(a) shows how \mathcal{N}_{out} becomes suppressed when sending more and more thermal photons into the JPA. At some point, the JPA cannot squeeze the incoming field below the vacuum anymore and the output state is no longer entangled. For constant temperature, Fig. 3(b) shows how \mathcal{N}_{out} increases with increasing signal gain from zero to a value $\mathcal{N}_{\text{out,max}} = 0.55 \pm 0.04$ at 10 dB signal gain. This behavior is in good agreement with the negativity $\mathcal{N}_{\text{calc}}$ calculated from the dual-path reconstructed input state. Again, we observe a suppression for large thermal fields sent into the JPA. Our results confirm the expectation²⁹ that the degree of squeezing at the beam splitter input determines the amount of entanglement generated between the output paths. However, since $\mathcal{N}_{\text{calc}}$ is generally slightly lower than \mathcal{N}_{out} , we conclude that either the dual-path reconstruction underestimates the squeezing at the beam splitter input or the reference-state method ignores a small amount of spurious classical correlations between the two paths. Both effects are consistent with the data shown in Fig. 3(a), where at constant signal gain,

the curve measured with the reference-state method at the beam splitter output converges for high temperatures to that calculated from the dual-path reconstructed input state. We finally note that the path-entangled state is expected to be a two-mode squeezed state with two additional local squeezing operations applied to it²⁹. Since local operations do not change the amount of entanglement, the negativity $\mathcal{N}_{\text{out,max}} = 0.55 \pm 0.04$ implies that the two-mode squeezed state before the two local operations would have a variance squeezed by 3.2 dB below that of the two-mode vacuum.

In summary, we present clear evidence for path entanglement generated by combining two frequency-degenerate continuous-variable microwave fields, the vacuum and the squeezed vacuum, in a beam splitter. For an input state squeezed 4.9 ± 0.2 dB below the vacuum, we observe a maximum negativity $\mathcal{N}_{\text{out,max}} = 0.55 \pm 0.04$ at 10 dB JPA signal gain. Our experiments bring the exciting quantum physics of entangled propagating electromagnetic fields to the technologically highly attractive microwave domain. In this way, they open up new and exciting perspectives towards microwave quantum teleportation, quantum communication, and quantum radar³⁰.

The authors thank Christopher Eichler for discussions. We acknowledge support from the Deutsche Forschungsgemeinschaft via the Sonderforschungsbereich 631, the German excellence initiative via the ‘Nanosystems Initiative Munich’ (NIM), from the EU projects SOLID, CC-QED and PROMISCE, from MEXT Kakenhi “Quantum Cybernetics”, the JSPS through its FIRST Program, the

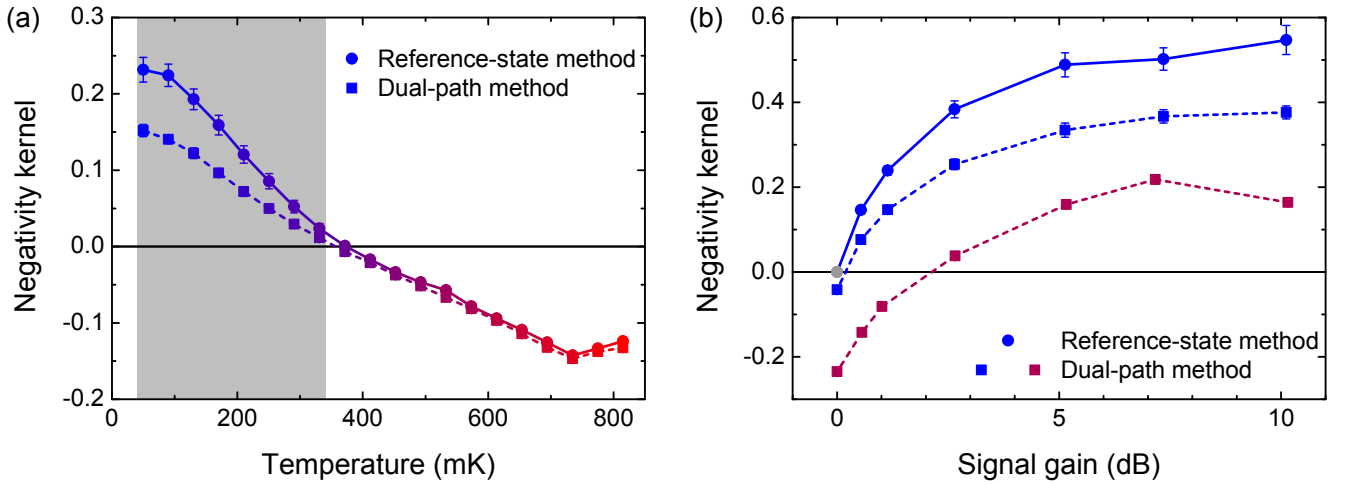


FIG. 3. Quantitative analysis of the path entanglement generated in our experiments. The negativities \mathcal{N}_{out} , $\mathcal{N}_{\text{calc}}$ are the maxima of the corresponding negativity kernels \mathcal{N}_{out} , $\mathcal{N}_{\text{calc}}$ and 0. Circular symbols: \mathcal{N}_{out} data at the beam splitter output. Square symbols: $\mathcal{N}_{\text{calc}}$ calculated from the reconstructed input state. The lines are guides to the eye. (a) Negativity kernel versus attenuator temperature (color code) at 1 dB signal gain. For the data points in the shaded area, the witness matrix²⁶ confirms entanglement. (b) Negativity kernel versus the JPA signal gain. The blue (red) curves are recorded at 50 mK (573 mK). Grey point: negativity of the reference state, assumed to be zero.

Project for Developing Innovation Systems of MEXT, the NICT Commissioned Research, EPSRC EP/H050434/1,

Basque Government IT472-10, and Spanish MICINN FIS2009-12773-C02-01.

* Edwin.Menzel@wmi.badw-muenchen.de

- ¹ R. Horodecki, P. Horodecki, M. Horodecki, and K. Horodecki, *Rev. Mod. Phys.* **81**, 865 (2009).
- ² M. Born, *The Born-Einstein Letters* (Walker and Company, New York, 1971).
- ³ A. Einstein, B. Podolsky, and N. Rosen, *Phys. Rev.* **47**, 777 (1935).
- ⁴ J. Raimond, M. Brune, and S. Haroche, *Rev. Mod. Phys.* **73**, 565 (2001).
- ⁵ S. L. Braunstein and P. van Loock, *Rev. Mod. Phys.* **77**, 513 (2005).
- ⁶ Z. Y. Ou, S. F. Pereira, H. J. Kimble, and K. C. Peng, *Phys. Rev. Lett.* **68**, 3663 (1992).
- ⁷ R. J. Schoelkopf and S. M. Girvin, *Nature* **451**, 664 (2008).
- ⁸ J. Clarke and F. K. Wilhelm, *Nature* **453**, 1031 (2008).
- ⁹ M. Mariani, H. Wang, T. Yamamoto, M. Neeley, R. C. Bialczak, Y. Chen, M. Lenander, E. Lucero, A. D. O'Connell, D. Sank, M. Weides, J. Wenner, Y. Yin, J. Zhao, A. N. Korotkov, A. N. Cleland, and J. M. Martinis, *Science* **334**, 61 (2011).
- ¹⁰ A. Wallraff, D. I. Schuster, A. Blais, L. Frunzio, R.-S. Huang, J. Majer, S. Kumar, S. M. Girvin, and R. J. Schoelkopf, *Nature* **431**, 162 (2004).
- ¹¹ T. Niemczyk, F. Deppe, H. Huebl, E. P. Menzel, F. Hocke, M. J. Schwarz, J. J. Garcia-Ripoll, D. Zueco, T. Hümmer, E. Solano, A. Marx, and R. Gross, *Nature Phys.* **6**, 772 (2010).
- ¹² J. Majer, J. M. Chow, J. M. Gambetta, J. Koch, B. R. Johnson, J. A. Schreier, L. Frunzio, D. I. Schuster, A. A. Houck, A. Wallraff, A. Blais, M. H. Devoret, S. M. Girvin, and R. J. Schoelkopf, *Nature* **449**, 443 (2007).

- ¹³ M. A. Sillanpää, J. I. Park, and R. W. Simmonds, *Nature* **449**, 438 (2007).
- ¹⁴ T. Yamamoto, Yu. A. Pashkin, O. Astafiev, Y. Nakamura, and J. S. Tsai, *Nature* **425**, 941 (2003).
- ¹⁵ J. H. Plantenberg, P. C. de Groot, C. J. P. M. Harmans, and J. E. Mooij, *Nature* **447**, 836 (2007).
- ¹⁶ M. Ansmann, H. Wang, R. C. Bialczak, M. Hofheinz, E. Lucero, M. Neeley, A. D. O'Connell, D. Sank, M. Weides, J. Wenner, A. N. Cleland, and J. M. Martinis, *Nature* **461**, 504 (2009).
- ¹⁷ M. Mariani, E. P. Menzel, F. Deppe, M. Á. Araque Caballero, A. Baust, T. Niemczyk, E. Hoffmann, E. Solano, A. Marx, and R. Gross, *Phys. Rev. Lett.* **105**, 133601 (2010).
- ¹⁸ E. P. Menzel, F. Deppe, M. Mariani, M. Á. Araque Caballero, A. Baust, T. Niemczyk, E. Hoffmann, A. Marx, E. Solano, and R. Gross, *Phys. Rev. Lett.* **105**, 100401 (2010).
- ¹⁹ D. Bozyigit, C. Lang, L. Steffen, J. M. Fink, C. Eichler, M. Baur, R. Bianchetti, P. J. Leek, S. Filipp, M. P. da Silva, A. Blais, and A. Wallraff, *Nature Phys.* **7**, 154 (2011).
- ²⁰ F. Mallet, M. A. Castellanos-Beltran, H. S. Ku, S. Glancy, E. Knill, K. D. Irwin, G. C. Hilton, L. R. Vale, and K. W. Lehnert, *Phys. Rev. Lett.* **106**, 220502 (2011).
- ²¹ C. Eichler, D. Bozyigit, C. Lang, M. Baur, L. Steffen, J. M. Fink, S. Filipp, and A. Wallraff, *Phys. Rev. Lett.* **107**, 113601 (2011).
- ²² C. M. Wilson, G. Johansson, A. Pourkabirian, M. Simoen, J. R. Johansson, T. Duty, F. Nori, and P. Delsing, *Nature* **479**, 376 (2011).

- ²³ E. Flurin, N. Roch, F. Mallet, M. H. Devoret, and B. Huard, (2012), arXiv:1204.0732.
- ²⁴ E. Hoffmann, F. Deppe, T. Niemczyk, T. Wirth, E. P. Menzel, G. Wild, H. Huebl, M. Mariani, T. Weiß, A. Lukashenko, A. P. Zhuravel, A. V. Ustinov, A. Marx, and R. Gross, *Appl. Phys. Lett.* **97**, 222508 (2010).
- ²⁵ C. Eichler, D. Bozyigit, C. Lang, L. Steffen, J. Fink, and A. Wallraff, *Phys. Rev. Lett.* **106**, 220503 (2011).
- ²⁶ E. Shchukin and W. Vogel, *Phys. Rev. Lett.* **95**, 230502 (2005).
- ²⁷ G. Adesso and F. Illuminati, *Phys. Rev. A* **72**, 032334 (2005).
- ²⁸ T. Yamamoto, K. Inomata, M. Watanabe, K. Matsuba, T. Miyazaki, W. D. Oliver, Y. Nakamura, and J. S. Tsai, *Appl. Phys. Lett.* **93**, 042510 (2008).
- ²⁹ M. S. Kim, W. Son, V. Bužek, and P. L. Knight, *Phys. Rev. A* **65**, 032323 (2002).
- ³⁰ M. Lanzagorta, in *Quantum Radar*, Synthesis Lectures on Quantum Computing, Vol. 5, edited by M. Lanzagorta and J. Uhlmann (Morgan & Claypool Publishers, 2012).

Supplementary

I. EXPERIMENTAL DETAILS

A. The flux driven Josephson parametric amplifier

We generate squeezed states using a flux driven Josephson parametric amplifier³¹ (JPA). Micrographs of the device used in our experiments are shown in Figs. S1(a)–(d), a circuit diagram is displayed in Fig. S1(e). In order to achieve a parametric effect, the resonance frequency f_{dc} of a quarter wavelength superconducting coplanar waveguide resonator (external quality $Q_{ext} = 312$) is modulated at $2f_{dc}$. To this end, a dc superconducting quantum interference device (SQUID) – a superconducting loop interrupted by two Josephson

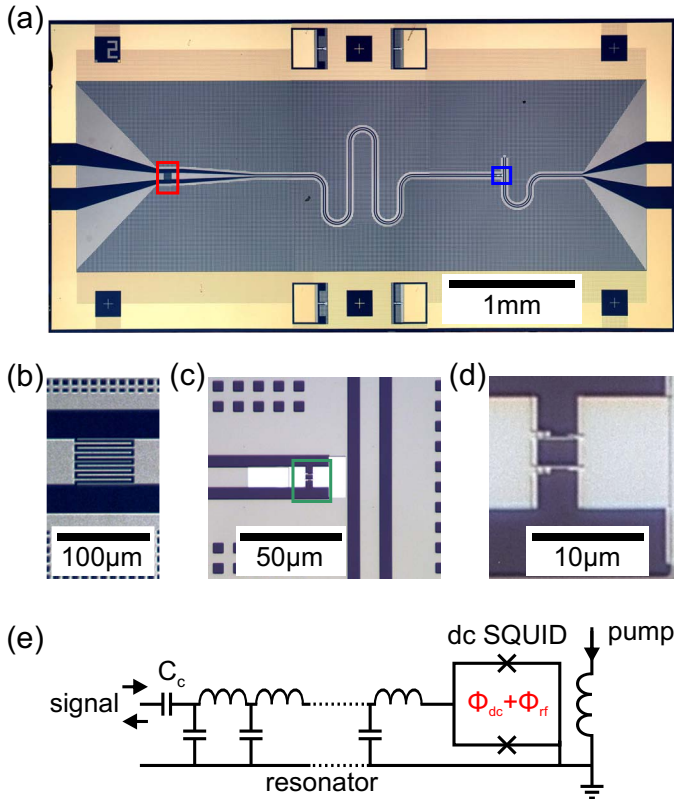


Fig. S1. Flux driven Josephson parametric amplifier used in our experiments. (a) Sample chip. (b) Zoom-in of the region marked with the red rectangle in panel (a), showing the coupling capacitor C_c . (c) Pump line and dc SQUID. Zoom-in of the region marked with the blue rectangle in panel (a), showing the pump line and the dc SQUID. (d) Zoom-in of the region marked with the green rectangle in panel (c), showing the dc SQUID. (e) Circuit diagram.

junctions – is inserted between the center conductor and the ground plane at the shorted end of the resonator. Because the SQUID acts as a flux-tunable inductor, the resonance frequency of the resonator can be changed by applying an external magnetic field. Via an external coil, we first set a quasistatic bias corresponding to a JPA operating frequency of $f_0 = 5.637$ GHz (see Fig. S2). The fast modulation at $2f_0$, also referred to as the pump tone, is then applied in a pulsed fashion (see Sec. II A) via an on-chip antenna. We determine the isolation between antenna and resonator to be at least 28 dB at the signal frequency f_0 .

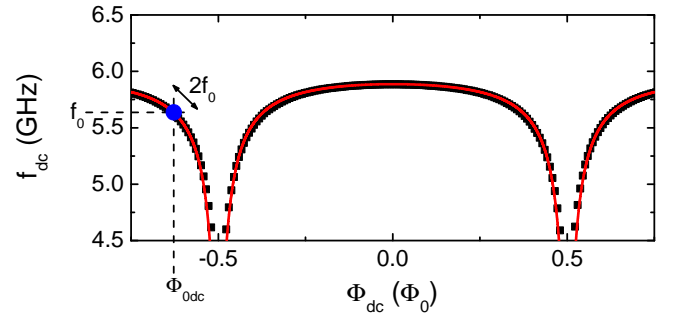


Fig. S2. JPA resonance frequency f_{dc} as a function of the applied dc flux Φ_{dc} . Black symbols: data. Red line: fit. Blue dot: operating point $f_0 = 5.637$ GHz.

Resonator and antenna are made of a 50 nm thick Nb film. At the contacts, 95 nm of gold on a 5 nm titanium bonding layer are deposited on top. As substrate, we use thermally oxidized (300 nm) silicon with a thickness of 300 μm . The dc SQUID is fabricated in the last step using aluminum technology and shadow evaporation. The Al electrodes have a thickness of 50 nm each. From Fig. S2, we estimate a Josephson coupling energy $E_J/h = 650$ GHz for each junction, where $h = 6.63 \times 10^{-34}$ Js is the Planck constant. The sample chip is placed between two small alumina printed circuit boards inside a gold-plated copper box.

B. The 180° hybrid ring microwave beam splitter

Microwave beam splitters divide an input signal while possibly adding phases to their outputs. However, in order to be lossless, matched, and reciprocal, these devices must necessarily have four ports³². In a quantum mechanical picture, this implies that a second, possibly hidden input port is always present³³. A sketch of the 180° hybrid ring microwave beam splitter used in this work is shown in Fig. S3. It is a commercially fabricated device based on gold microstrip transmission lines on a dielectric substrate encased in a copper housing. Its functionality is best understood as follows: at a wavelength λ , the signals incident at the input ports form an interference pattern in the ring with antinodes at the output ports and nodes at the input ports³². This was

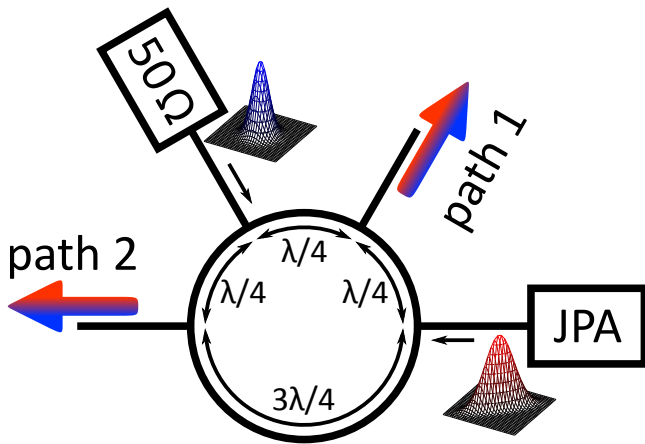


Fig. S3. Schematic sketch of the 180° hybrid ring microwave beam splitter used in our experiments. The split signals from the JPA acquire a 180° phase shift with respect to each other, while the split signals from the 50Ω termination remain in phase.

experimentally demonstrated in Ref. 34, where also typical transmission characteristics are shown. The signals from the two input ports are evenly split and superposed in the two output ports. In this superposition, the component from one of the inputs acquires a 180° phase shift between the output ports, while that from the other one remains in phase. The center frequency of our hybrid ring is 5.75 GHz. Within our measurement bandwidth of $2 \times BW_{\text{filter}} = 2 \times 489$ kHz centered at the JPA operating frequency f_0 (see also Fig. S8), our hybrid ring still has a coupling of 3.5 dB between input and output ports and an isolation of at least 38 dB between any two input or output ports. The magnitude imbalance between the two output ports is only 0.03 dB. For a JPA emitting a squeezed state and a 50Ω termination emitting vacuum fluctuations into the input ports of our hybrid ring, the state in the beam splitter output ports is expected to be path-entangled³⁵.

C. The cross correlation detector

In Fig. S4, a simplified sketch of the cross correlation detector is shown. Along each path, the signal emerging from the hybrid ring is linearly amplified, filtered, down-converted to an intermediate frequency $f_{\text{IF}} = 11$ MHz, and digitized at a sampling rate of 150 MHz by 16 bit analog-to-digital converters. The IQ-mixers used for down-conversion are biased by a strong local oscillator at 5.626 GHz and split each output signal into its in-phase ($I_{1,2}$) and quadrature ($Q_{1,2}$) components – therefore four ADCs are required. The digitized signals are finally fed into an FPGA logic (details can be found in Sec. II A) which computes all correlations up to the fourth moment in amplitude in real time. Phase synchronization is guaranteed by using a joint local oscillator for down-

conversion and referencing the clock of the FPGA logic to that of the local oscillator.

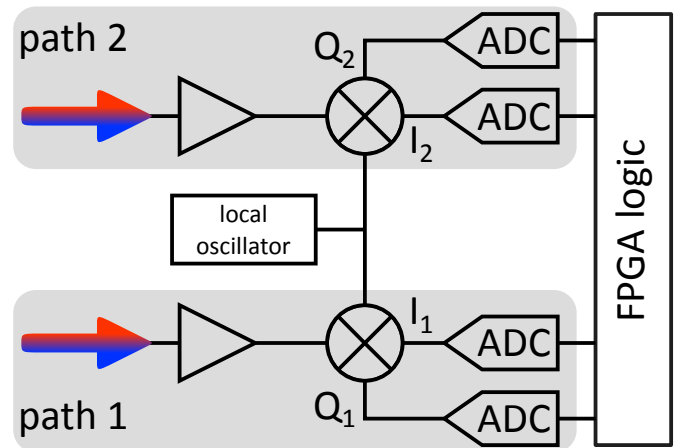


Fig. S4. Sketch of the cross correlation detector. Colored arrows: output signals from the hybrid ring. Triangular symbols: amplifiers. Circles with crosses: IQ-mixers.

D. Detailed setup

A detailed setup of the experiment is shown in Fig. S5. JPA, 50Ω terminated hybrid ring, and measurement circulator are anchored to the base temperature plate of a dilution refrigerator, whose temperature is stabilized to 50 mK measured on the JPA sample box. Near the 50Ω termination of the hybrid ring, we measure a temperature of 40 mK. The JPA signal and pump lines are heavily attenuated at various temperature stages. The coldest attenuator of the signal line is only weakly coupled to the base plate and the lower step exchanger of the fridge. Its temperature can therefore be controlled in the range $T_{\text{att}} = 50 - 800$ mK, while all other components retain a stable temperature. This attenuator constitutes a broadband microwave black body emitter, which is used to calibrate the gains of the amplification paths in a Planck spectroscopy experiment³³. The total power of each amplification path detected at the ADCs is

$$P_{1,2}(T_{\text{att}}) = \frac{\langle I_{1,2}^2 \rangle + \langle Q_{1,2}^2 \rangle}{R} = \frac{\kappa G_{1,2}}{R} \left[\frac{1}{2} \coth \left(\frac{hf_0}{2k_{\text{B}}T_{\text{att}}} \right) + n_{1,2} \right], \quad (1)$$

where $R = 50\Omega$ is the input resistance of the ADCs and $k_{\text{B}} = 1.38 \times 10^{-23}$ J/K the Boltzmann constant. The product of the gain $G_{1,2}$ and the photon number conversion factor $\kappa \equiv R \times 2 \times BW_{\text{filter}} \times hf_0 = 1.83 \times 10^{-16}$ V² relates the measured autocorrelations $\langle I_{1,2}^2 \rangle$ and $\langle Q_{1,2}^2 \rangle$, which have units of V², to the number of photons of frequency f_0 referred to the attenuator. The gain $G_{1,2}$ and the number of noise photons added by each amplification

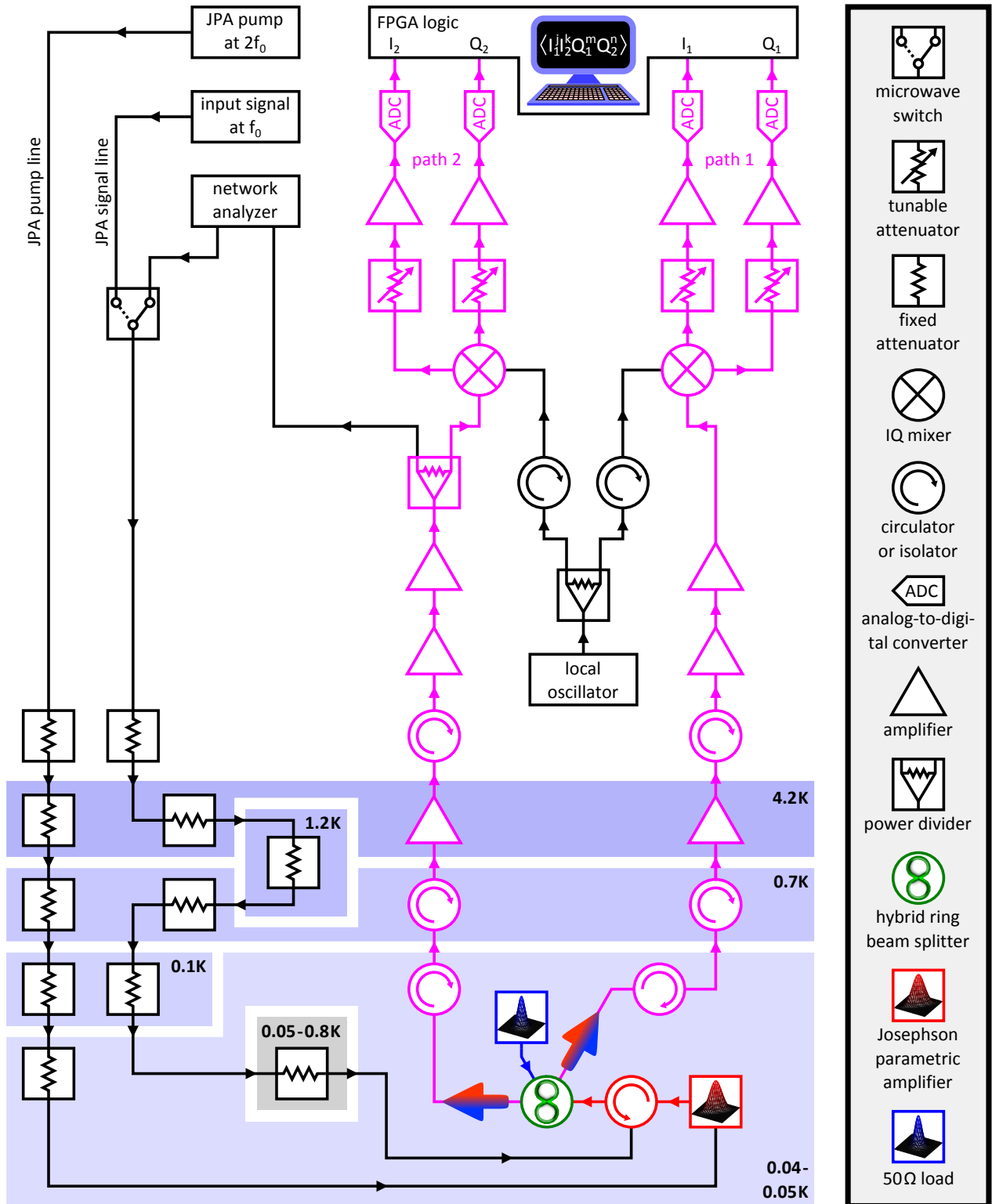


Fig. S5. Detailed experimental setup. The bold numbers indicate the temperatures of the corresponding colored boxes. The two amplification and detection paths are marked with magenta color. The colored arrows denote the path entangled output state of the beam splitter.

path, $n_{1,2}$, are retrieved from fitting Eq. (1) to the experimentally recorded autocorrelations. For pedagogical reasons, all formulas given in this manuscript assume equal gains and losses for the I and Q branches within each path. However, in the actual evaluation of the data, we do not make this assumption. We model the losses with beam splitters and also account for temperature gradients along our cables. In this way, we make individual fits for the dependence of $\langle I_1^2 \rangle$, $\langle I_2^2 \rangle$, $\langle Q_1^2 \rangle$, and $\langle Q_2^2 \rangle$ on T_{att} . As an example, we show data and fit for $\langle I_1^2 \rangle$ in Fig. S6. We first note that from this figure, we immediately see that the number of thermal photons in the mode f_0 is negligible at 40 – 50 mK. Furthermore, with a total loss of 1.8 dB between attenuator and beam splitter input, we retrieve $G_{\text{d1}}/2 = 116.5$ dB and $n_{\text{d1}} = 24.3$ photons. Here, the index “d” denotes that $G_{\text{d1}}/2$ and n_{d1} are referred to the input of the hybrid ring. From our reference-state analysis described in Sec. III B, we obtain, with respect to the beam splitter output ports, noise temperatures of 3.00 K and 3.27 K for the two amplification paths. Considering that our beam splitter reduces the input signal by 3.5 dB, the value of 3.00 K is in very good agreement with that of n_{d1} quoted above.

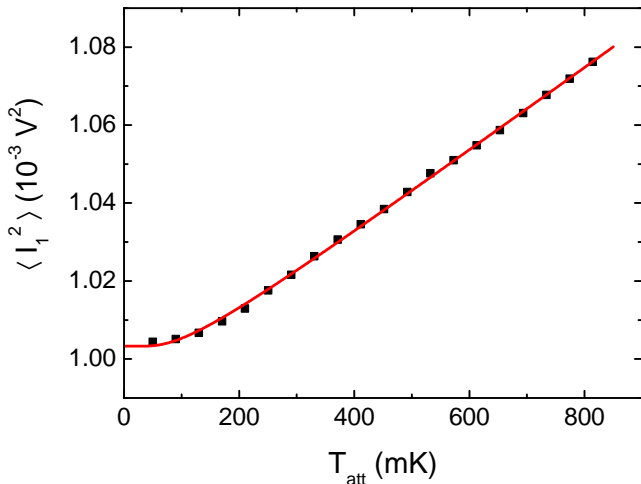


Fig. S6. Gain calibration. Dependence of the second moment $\langle I_1^2 \rangle$ on the temperature of the attenuator temperature T_{att} . Black symbols: data. Red line: fit.

Apart from the key functional elements described in Sec. I C, the amplification paths contain isolating elements at various temperature stages to avoid spurious correlated noise contributions. Furthermore, tunable attenuators after the IQ-mixers allow for a prebalancing of the four channels. The JPA pump and signal microwave sources, the local oscillator for the IQ mixers, and the clock for the ADCs and the FPGA logic are synchronized with a Rubidium-based 10 MHz source. The vector network analyzer is used to measure the JPA operating point, signal gain, and idler gain. Finally, in addition to the elements shown in Fig. S5, several components such as mechanical microwave switches, power dividers, and a spectrum analyzer are used in the real setup. We omit

these elements in our discussion here since they serve purely technical purposes (e.g., debugging or switching to other experiments) and are not essential for the functionality of the cross correlation detector and the entanglement detection.

II. PROTOCOL FOR CROSS CORRELATION MEASUREMENTS

A. Data acquisition

In our experiments, we use either a squeezed state or a coherent state at one of the beam splitter inputs, while a vacuum state is always incident at the second one. During measurements on squeezed states, the JPA pump at frequency $2f_0$ is operated in pulsed mode. Similarly, we also use pulsed probe signals when measuring coherent states of frequency f_0 . The rise and fall times of the pulse envelopes are approximately 10 ns each. As shown in Fig. S7, the measurement window always contains an off-region as a reference in addition to the signal. At low enough temperatures, this reference state can be considered as the vacuum (see also Sec. III B).

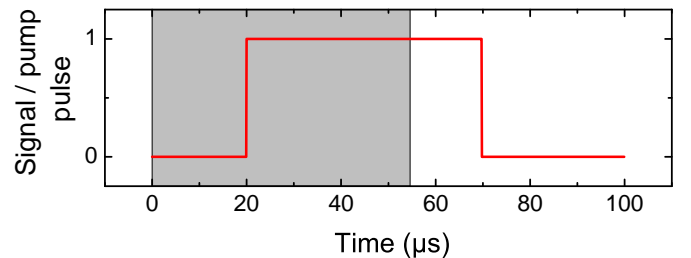


Fig. S7. Measurement protocol for squeezed and coherent states. During the high time (“1”) of the pulse envelope, either the coherent signal or the JPA pump tone is on, during the low time (“0”) both are off. The shaded area denotes the measurement window.

For the dual-path reconstruction and the entanglement detection, the orthogonal I and Q quadratures of the noisy signal have to be recorded for both paths and products of the type $\langle I_1^j I_2^k Q_1^m Q_2^n \rangle$, where $j+k+m+n \leq 4$ and $j, k, m, n \in \mathbb{N}_0$, need to be calculated for each recorded data point. However, the presence of the amplifier noise of our paths requires significant averaging. As a consequence, data transfer rate and computation time become a serious bottleneck in a computer-based acquisition system. By streaming the data from the ADCs directly into an FPGA logic, we solve these problems and are able to perform the moment calculations in real time.

Data acquisition is triggered every 100 μs . For each trigger event, 8192 consecutive points are digitized in each of the four channels at a rate of 150 MHz. As shown in Fig. S7, this results in a duty cycle of 54.6%. The data is streamed directly into the FPGA, where it first

passes a gain balancing and a digital down-conversion stage. The latter also allows for fine-tuning of the phase difference between the two paths to 180° and for correction for phase imperfections of the IQ-mixer. In the next step, the number of data points is reduced to 512 with a digital cascaded integrator comb (CIC) filter. The final bandwidth is determined by the subsequent digital finite impulse response (FIR) filter. These filters also determine the measurement bandwidth (noise bandwidth) of $2 \times BW_{\text{filter}} = 2 \times 489 \text{ kHz}$ of the cross correlation detector. The corresponding transmission characteristics is shown in Fig. S8. We note that one of the key advantages of digital filtering is that the frequency dispersion is flat and that the transmission characteristics are exactly equal for all four detection channels. Furthermore, for JPA signal gains up to 20 dB, the JPA bandwidth is larger than the measurement bandwidth.

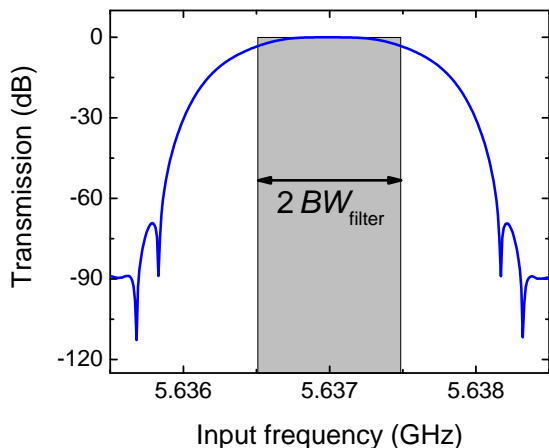


Fig. S8. Measured transmission characteristics of the cross correlation detector.

Finally, the moments up to fourth order in amplitude are calculated. For each moment and each data point, the average over a specified number of trigger events, in the following called ensemble average, is stored inside the FPGA. Figure S9 shows typical time traces for selected second moments of a squeezed state averaged over 5×10^5 traces. Since the phase angle in this example is chosen to be 0° , $\langle Q_1^2 \rangle$ increases significantly above the vacuum level and $\langle I_1^2 \rangle$ decreases below the vacuum level as expected. The cross moment $\langle I_1 I_2 \rangle$ shows the characteristic cancellation of the uncorrelated noise contributions of the amplification paths, which lies at the heart of the dual-path tomography. A Wigner function reconstruction based on this dataset is shown in Fig. S11(b).

B. Dual-path tomography of coherent states

We first test the dual-path setup against coherent states of frequency $f_0 = 5.637 \text{ GHz}$ from a microwave signal generator. The JPA pump is off in these measurements. In Fig. S10, we show the photon number $n \equiv \langle \hat{a}^\dagger \hat{a} \rangle$

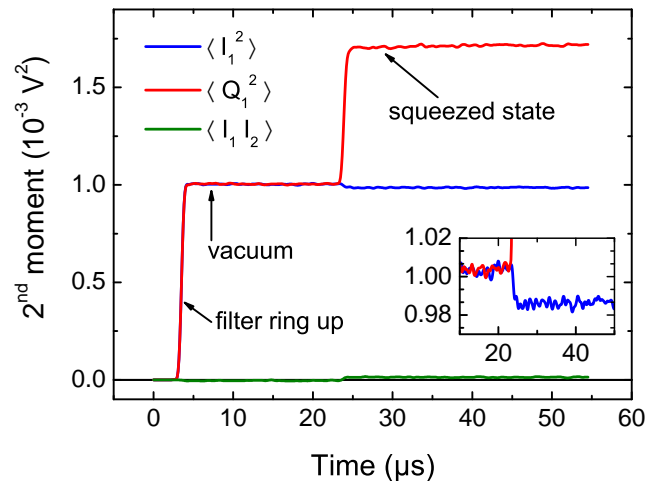


Fig. S9. Typical averaged time traces of selected second moments from a squeezed state measurement with 0° phase and for 10 dB signal gain. Each averaged trace consists of 5×10^5 single traces. The rise time of 650 ns is determined by the digital filters. The step between JPA pump off (vacuum) and on (squeezed state) is shifted by $4 \mu\text{s}$ with respect to the pulse shown in Fig. S7 because of a delay due to filtering.

and amplitude $\alpha \equiv \langle \hat{a} \rangle$ extracted from the reconstructed moments against the power P_{gen} at the output of the signal generator. Here, \hat{a}^\dagger and \hat{a} are the field operators of the input state as defined in Sec. III A. The expected linear and square root dependences, $n(P_{\text{gen}}) = AP_{\text{gen}}$ and $\alpha(P_{\text{gen}}) = B\sqrt{P_{\text{gen}}}$, are clearly reproduced. Within an error bar of less than two percent, B is the square root of A for independent fits.

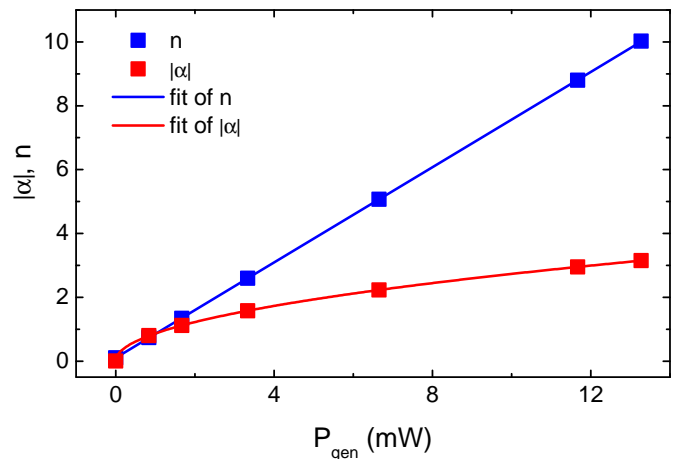


Fig. S10. Coherent state reconstruction. Photon number n and amplitude $|\alpha|$ as a function of the signal generator power P_{gen} .

C. Phase stabilization protocol

The phase stability between signal/pump and local oscillator is better than $\pm 0.3^\circ$ for 5×10^5 traces. Hence, reconstructions based on such a number of averages exhibit very good phase control as shown in Fig. S11. However, for quantifying the path entanglement properties, an average over $8 \times 10^6 - 3 \times 10^7$ traces is necessary to reduce the influence of the noise added by each amplification path to a negligible amount. In such measurements, the phase stability of our setup is not sufficient. For this reason, we record the data in 5×10^5 trace portions and adjust the relative phase between signal/pump and local oscillator in a way that phase drifts are compensated. In particular, the data shown in Fig. 3 of the main text are recorded in this fashion.

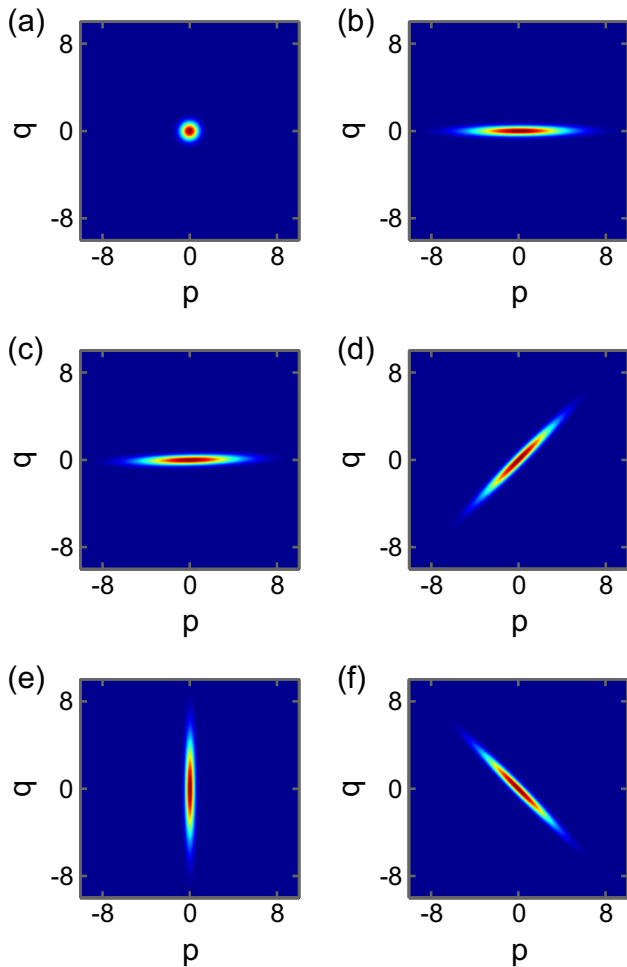


Fig. S11. Phase control for squeezed state reconstruction. Wigner functions of (a) the vacuum, (b) a squeezed state at 0° , (c) a squeezed state at 1° , (d) a squeezed state at 45° , (e) a squeezed state at 90° , and (f) a squeezed state at 135° . The number of averaged traces is 5×10^5 . The residual thermal population of the vacuum is 0.102 ± 0.005 photons. For the squeezed state, the JPA signal gain is 10 dB and the reconstructed photon number $n = 8.67$ varies by approximately 0.5% for the different phase angles.

III. THEORY: DUAL-PATH TOMOGRAPHY AND ENTANGLEMENT DETECTION

In the optical domain, efficient single photon detectors and optical homodyning are established measurement techniques for quantum correlations³⁶. However, despite recent efforts³⁷⁻³⁹, the translation of these methods to the microwave regime remains difficult because of the low photon energy. Therefore, quantum microwave reconstruction based on off-the-shelf noisy linear amplifiers and cross-correlation techniques, the cross-correlation detector⁴⁰, was proposed and experimentally implemented^{40,41}. Later, a second reconstruction technique using only a single amplification path and deconvolution based on a reference measurement was demonstrated^{42,43}. In what follows, we describe the mathematical details of these methods, which we adopted to the needs of our experiments: the reconstruction of the state incident at the input port and the detection of entanglement between signals propagating in the output paths of the beam splitter.

A. Dual-path reconstruction of the input state

For the input state reconstruction, we can make use of the beam splitter and cross correlations. As described below, we in this way cancel the amplifier noise obscuring the signals because the noise contributions of the two paths are independent. The functionality of microwave beam splitters is well-established for classical signals and was recently demonstrated also for the quantum regime^{33,40,41}.

For quantum microwaves, we need to take into account the orthogonal signal quadratures $I_{1,2}$ and $Q_{1,2}$. These are real valued voltages measured at the outputs of the IQ-mixers (see Fig. S4 and Fig. S5). We can now define the dimensionless complex envelope functions

$$\xi_{1,2} \equiv (I_{1,2} + iQ_{1,2})/\sqrt{\kappa}, \quad (2)$$

where κ is the photon number conversion factor introduced in Sec. ID. The corresponding operators,

$$\hat{\xi}_{1,2} \equiv (\hat{I}_{1,2} + i\hat{Q}_{1,2})/\sqrt{\kappa}, \quad (3)$$

can, in this situation, be expressed as⁴⁴

$$\hat{\xi}_{1,2} = \hat{C}_{1,2} + \hat{v}_{1,2}^\dagger. \quad (4)$$

Here, $\hat{C}_{1,2}$ is the bosonic annihilation operator of the input signal into the IQ-mixer. The noise added by the latter is represented by its bosonic creation operator $\hat{v}_{1,2}^\dagger$. We now have $[\hat{\xi}_{1,2}, \hat{\xi}_{1,2}^\dagger] = 0$, and the correlations $\langle \hat{\xi}_1^{j'} (\hat{\xi}_1^\dagger)^{m'} \hat{\xi}_2^{k'} (\hat{\xi}_2^\dagger)^{n'} \rangle = \langle (\hat{\xi}_1^\dagger)^{m'} \hat{\xi}_1^{j'} (\hat{\xi}_2^\dagger)^{n'} \hat{\xi}_2^{k'} \rangle$ can be expressed in terms of the measured $\langle I_1^j I_2^k Q_1^m Q_2^n \rangle$ via Eq. (2) by identifying $\hat{\xi}_{1,2}$ with $\xi_{1,2}$ and $\hat{\xi}_{1,2}^\dagger$ with $\xi_{1,2}^*$. We note that, while in general, $j', k', m', n', j, k, m, n \in \mathbb{N}_0$, in

this manuscript we restrict ourselves to $j + k + m + n \leq 4$ or, equivalently, $j' + k' + m' + n' \leq 4$.

Using the beam splitter relations and the standard quantum model for linear amplifiers⁴⁵, we can now write

$$\hat{\xi}_1 = \sqrt{\frac{G_{d1}}{2}}(+\hat{a} + \hat{v}) + \sqrt{G_{d1} - 1}\hat{h}_1^\dagger + \hat{v}_1^\dagger \quad (5)$$

$$\hat{\xi}_2 = \sqrt{\frac{G_{d2}}{2}}(-\hat{a} + \hat{v}) + \sqrt{G_{d2} - 1}\hat{h}_2^\dagger + \hat{v}_2^\dagger \quad (6)$$

for our setup. Here, \hat{a} and \hat{v} are bosonic annihilation operators. They describe the modes incident on the signal and the $50\ \Omega$ terminated input port of the beam splitter, respectively. The noise fields added by each amplification path are represented by the bosonic creation operators $\hat{h}_{1,2}^\dagger$. Their effective temperature is mainly determined by the noise temperatures of the cold HEMT amplifiers and the cable losses between beam splitter and HEMT amplifier. $G_{d1,2}$ are the gains of the output paths calibrated as described in Sec. ID. In order to simplify the notation, we also define the operators

$$\hat{V}_{1,2} \equiv \sqrt{\frac{2}{G_{d1,2}}} \left(\sqrt{G_{d1,2} - 1} \hat{h}_{1,2} + \hat{v}_{1,2} \right) \quad (7)$$

$$\hat{S}_{1,2} \equiv \sqrt{\frac{2}{G_{d1,2}}} \hat{\xi}_{1,2}. \quad (8)$$

We note that $\hat{V}_{1,2}/\sqrt{2}$ is a bosonic operator, as $[\frac{\hat{V}_{1,2}}{\sqrt{2}}, \frac{\hat{V}_{1,2}^\dagger}{\sqrt{2}}] = 1$. In this way, we arrive at the simple expressions

$$\hat{S}_1 = +\hat{a} + \hat{v} + \hat{V}_1^\dagger \quad (9)$$

$$\hat{S}_2 = -\hat{a} + \hat{v} + \hat{V}_2^\dagger. \quad (10)$$

We note that the operators $\hat{V}_{1,2}$, \hat{a} , and \hat{v} , and therefore also $\hat{S}_{1,2}$, are referred to the input of the beam splitter. With these definitions, we can generalize the dual-path state reconstruction technique, which we originally developed in Ref. 40, in a way that it becomes applicable to the experimental setup presented in this work. Making the reasonable assumptions that \hat{v} is a weak thermal state with a measured temperature of 40 mK and that

$$\langle \hat{V}_1 \rangle = \langle \hat{V}_2 \rangle = 0 \quad (11)$$

for the noise added by the amplification paths, we recursively obtain the signal moments

$$\begin{aligned} \langle (\hat{a}^\dagger)^l \hat{a}^m \rangle_{l_1, m_1} &= (-1)^{l-l_1+m-m_1} \langle (\hat{S}_1^\dagger)^{l_1} (\hat{S}_2^\dagger)^{l-l_1} \hat{S}_1^{m_1} \hat{S}_2^{m-m_1} \rangle \\ &- \sum_{k_1=0}^{l_1} \sum_{k_2=0}^{l-l_1} \sum_{j_1=0}^{m_1} \sum_{j_2=0}^{m-m_1-1} \sum_{k'_1=0}^{l_1-k_1} \sum_{k'_2=0}^{l-l_1-k_2} \sum_{j'_1=0}^{m_1-j_1} \sum_{j'_2=0}^{m-m_1-j_2} \binom{l_1}{k_1} \binom{l-l_1}{k_2} \binom{m_1}{j_1} \binom{m-m_1}{j_2} \\ &\times \binom{l_1-k_1}{k'_1} \binom{l-l_1-k_2}{k'_2} \binom{m_1-j_1}{j'_1} \binom{m-m_1-j_2}{j'_2} (-1)^{l-l_1+m-m_1+j_2+k_2} \\ &\times \langle (\hat{a}^\dagger)^{k_1+k_2} \hat{a}^{j_1+j_2} \rangle \langle (\hat{v}^\dagger)^{k'_1+k'_2} \hat{v}^{j'_1+j'_2} \rangle \langle \hat{V}_1^{l_1-k_1-k'_1} (\hat{V}_1^\dagger)^{m_1-j_1-j'_1} \rangle \langle \hat{V}_2^{l-l_1-k_2-k'_2} (\hat{V}_2^\dagger)^{m-m_1-j_2-j'_2} \rangle \\ &- \sum_{k_1=0}^{l_1} \sum_{k_2=0}^{l-l_1} \sum_{j_1=0}^{m_1-1} \sum_{k'_1=0}^{l_1-k_1} \sum_{k'_2=0}^{l-l_1-k_2} \sum_{j'_1=0}^{m_1-j_1} \binom{l_1}{k_1} \binom{l-l_1}{k_2} \binom{m_1}{j_1} \binom{l-l_1-k_2}{k'_1} \binom{m_1-j_1}{k'_2} \binom{m_1-j_1}{j'_1} \\ &\times (-1)^{l-l_1+k_2} \langle (\hat{a}^\dagger)^{k_1+k_2} \hat{a}^{j_1+m-m_1} \rangle \langle (\hat{v}^\dagger)^{k'_1+k'_2} \hat{v}^{j'_1} \rangle \langle \hat{V}_1^{l_1-k_1-k'_1} (\hat{V}_1^\dagger)^{m_1-j_1-j'_1} \rangle \langle \hat{V}_2^{l-l_1-k_2-k'_2} \rangle \\ &- \sum_{k_1=0}^{l_1} \sum_{k_2=0}^{l-l_1-1} \binom{l_1}{k_1} \binom{l-l_1}{k_2} (-1)^{l-l_1+k_2} \langle (\hat{a}^\dagger)^{k_1+k_2} \hat{a}^m \rangle \langle \hat{V}_1^{l_1-k_1} \rangle \langle \hat{V}_2^{l-l_1-k_2} \rangle \\ &- \sum_{k_1=0}^{l_1-1} \binom{l_1}{k_1} \langle (\hat{a}^\dagger)^{k_1+l-l_1} \hat{a}^m \rangle \langle \hat{V}_1^{l_1-k_1} \rangle \end{aligned} \quad (12)$$

for $l, m, l_1, m_1 \in \mathbb{N}_0$ from the measured noisy correlations. In this process, we also have to compute the noise

moments

$$\begin{aligned}
\langle \hat{V}_1^r (\hat{V}_1^\dagger)^s \rangle &= \langle (\hat{S}_1^\dagger)^r \hat{S}_1^s \rangle \\
&- \sum_{k_1=0}^r \sum_{j_1=0}^{s-1} \sum_{k'_1=0}^{r-k_1} \sum_{j'_1=0}^{s-j_1} \binom{r}{k_1} \binom{s}{j_1} \binom{r-k_1}{k'_1} \binom{s-j_1}{j'_1} \langle (\hat{a}^\dagger)^{k'_1} \hat{a}^{j'_1} \rangle \langle (\hat{v}^\dagger)^{r-k_1-k'_1} \hat{v}^{s-j_1-j'_1} \rangle \langle \hat{V}_1^{k_1} (\hat{V}_1^\dagger)^{j_1} \rangle \\
&- \sum_{k_1=0}^{r-1} \binom{r}{k_1} \langle (\hat{a}^\dagger)^{r-k_1} \rangle \langle \hat{V}_1^{k_1} (\hat{V}_1^\dagger)^s \rangle,
\end{aligned} \tag{13}$$

$$\begin{aligned}
\langle \hat{V}_2^r (\hat{V}_2^\dagger)^s \rangle &= \langle (\hat{S}_2^\dagger)^r \hat{S}_2^s \rangle \\
&- \sum_{k_1=0}^r \sum_{j_1=0}^{s-1} \sum_{k'_1=0}^{r-k_1} \sum_{j'_1=0}^{s-j_1} \binom{r}{k_1} \binom{s}{j_1} \binom{r-k_1}{k'_1} \binom{s-j_1}{j'_1} (-1)^{k'_1+j'_1} \langle (\hat{a}^\dagger)^{k'_1} \hat{a}^{j'_1} \rangle \langle (\hat{v}^\dagger)^{r-k_1-k'_1} \hat{v}^{s-j_1-j'_1} \rangle \langle \hat{V}_2^{k_1} (\hat{V}_2^\dagger)^{j_1} \rangle \\
&- \sum_{k_1=0}^{r-1} \binom{r}{k_1} (-1)^{r-k_1} \langle (\hat{a}^\dagger)^{r-k_1} \rangle \langle \hat{V}_2^{k_1} (\hat{V}_2^\dagger)^s \rangle
\end{aligned} \tag{14}$$

associated with both amplification paths for $r + s > 1$ and $r, s \in \mathbb{N}_0$, again in a recursive fashion.

In other words, the formulas for the moments of order $l + m$ are established using those of the moments of order $l + m - 1$. The formulas obtained in this way are not unique, they depend on the specific choices of l_1 and m_1 . We find that the statistical uncertainty in our results is minimized by using the mean value of all formulas found for constant $l + m$.

From the reconstructed signal moments of Eq. (12), we can readily extract the squeezing below the vacuum in decibel,

$$\begin{aligned}
10 \log_{10} & \left(- \langle \hat{a}^2 \rangle e^{-i\phi} - \langle (\hat{a}^\dagger)^2 \rangle e^{i\phi} + 2 \langle \hat{a}^\dagger \hat{a} \rangle + 1 \right. \\
& \left. + \langle \hat{a} \rangle^2 e^{-i\phi} + \langle \hat{a}^\dagger \rangle^2 e^{i\phi} - 2 \langle \hat{a}^\dagger \rangle \langle \hat{a} \rangle \right). \tag{15}
\end{aligned}$$

Here, the angle ϕ is defined via the relation $\langle \hat{a}^2 \rangle - \langle \hat{a} \rangle^2 = |\langle \hat{a}^2 \rangle - \langle \hat{a} \rangle^2| e^{i\phi}$ and the argument of the logarithm is the ratio between the variance of the squeezed quadrature and the vacuum variance.

In the case of infinitely many reconstructed moments $\langle (\hat{a}^\dagger)^l \hat{a}^m \rangle$, the Wigner function $W(q, p)$ of an arbitrary state can be completely reconstructed. However, in this work we record these moments only up to fourth order, $l + m \leq 4$. As we find that the higher moments are consistent with those of Gaussian states, we are allowed to restrict ourselves to moments with $l + m \leq 2$. This enables us to use an analytical approach^{46,47}, which yields

$$W(q, p) = \frac{1}{\pi \sqrt{(\nu + 1/2)^2 - |\mu|^2}} \exp \left[- \frac{(\nu + 1/2) |\zeta - \langle \hat{a} \rangle|^2 - (\mu^*/2) (\zeta - \langle \hat{a} \rangle)^2 - (\mu/2) (\zeta^* - \langle \hat{a}^\dagger \rangle)^2}{(\nu + 1/2)^2 - |\mu|^2} \right], \tag{16}$$

with $\zeta \equiv q + ip$, $\mu \equiv \langle \hat{a}^2 \rangle - \langle \hat{a} \rangle^2$, and $\nu \equiv \langle \hat{a}^\dagger \hat{a} \rangle - |\langle \hat{a} \rangle|^2$. As explained in Sec. III A, we have chosen our definitions such that phase space variables q and p are dimensionless and their value represents the square root of a photon number. Since any Gaussian state can be written as a displaced squeezed thermal state, we can also extract the effective mode temperature analytically from the reconstructed input state moments^{46,47}. We note that this effective temperature contains contributions from the physical temperature and from losses.

B. Reference-state analysis of the output state moments

In order to detect the entanglement between the two paths independently from the dual-path reconstruction of the input state, we cannot assume that the hybrid ring is working as a beam splitter. We therefore follow a different route: we reconstruct the moments of the output state by means of a calibration against a well-known reference signal^{42,43}. The obvious choice for this reference signal is the two-mode vacuum. In this way, the beam splitter is treated as a black box device which, for a vacuum state at each input, produces uncorrelated vacuum states at each output port. This rather general assump-

tion holds well for the temperatures measured for attenuator and termination, 40 – 50 mK. In this situation, the complex envelope operator becomes

$$\hat{\xi}_1 = \sqrt{G_{r1}}\hat{s}_1 + \sqrt{G_{r1} - 1}\hat{h}_1^\dagger + \hat{v}_1^\dagger \quad (17)$$

$$\hat{\xi}_2 = \sqrt{G_{r2}}\hat{s}_2 + \sqrt{G_{r2} - 1}\hat{h}_2^\dagger + \hat{v}_2^\dagger. \quad (18)$$

Here, $\hat{s}_{1,2}$ is referred to the output of the beam splitter, and $G_{r1,2}$ is the effective gain of the amplification paths. Note that the $G_{r1,2}$ are numerically different from $G_{d1,2}$ because they do not contain the beam splitter losses. After defining the operators

$$\hat{V}_{1,2} \equiv \sqrt{\frac{1}{G_{r1,2}}} \left(\sqrt{G_{r1,2} - 1} \hat{h}_{1,2} + \hat{v}_{1,2} \right) \quad (19)$$

$$\hat{S}_{1,2} \equiv \sqrt{\frac{1}{G_{r1,2}}} \hat{\xi}_{1,2}, \quad (20)$$

we again arrive at the simplified expressions

$$\hat{S}_1 = \hat{s}_1 + \hat{V}_1^\dagger \quad (21)$$

$$\hat{S}_2 = \hat{s}_2 + \hat{V}_2^\dagger. \quad (22)$$

We now evaluate the correlations of the outputs of the two channels,

$$\begin{aligned} & \langle (\hat{S}_1^\dagger)^{l_1} \hat{S}_1^{m_1} (\hat{S}_2^\dagger)^{l_2} \hat{S}_2^{m_2} \rangle \\ &= \langle (\hat{s}_1^\dagger + \hat{V}_1^\dagger)^{l_1} (\hat{s}_1 + \hat{V}_1^\dagger)^{m_1} (\hat{s}_2^\dagger + \hat{V}_2^\dagger)^{l_2} (\hat{s}_2 + \hat{V}_2^\dagger)^{m_2} \rangle \\ &= \sum_{k_1=0}^{l_1} \sum_{k_2=0}^{l_2} \sum_{j_1=0}^{m_1} \sum_{j_2=0}^{m_2} \binom{l_1}{k_1} \binom{l_2}{k_2} \binom{m_1}{j_1} \binom{m_2}{j_2} \\ & \quad \times \langle (\hat{s}_1^\dagger)^{l_1-k_1} \hat{s}_1^{m_1-j_1} (\hat{s}_2^\dagger)^{l_2-k_2} \hat{s}_2^{m_2-j_2} \rangle \\ & \quad \times \langle \hat{V}_1^{k_1} (\hat{V}_1^\dagger)^{j_1} \hat{V}_2^{k_2} (\hat{V}_2^\dagger)^{j_2} \rangle. \end{aligned} \quad (23)$$

With the terms $\langle (\hat{s}_1^\dagger)^{l_1-k_1} \hat{s}_1^{m_1-j_1} (\hat{s}_2^\dagger)^{l_2-k_2} \hat{s}_2^{m_2-j_2} \rangle$, which can be calculated straightforwardly for our reference state, Eq. (23) forms a system of linear equations. The latter allows us to extract the noise terms $\langle \hat{V}_1^{k_1} (\hat{V}_1^\dagger)^{j_1} \hat{V}_2^{k_2} (\hat{V}_2^\dagger)^{j_2} \rangle$ related to our amplification paths by algebraic inversion. Once knowing these noise terms, we can extract the signal correlations for the squeezed state input again from Eq. (23) and algebraic inversion. We note that also more sophisticated reference states and device models, such as thermal states incident at a beam splitter, can be chosen as reference state. Depending on the pre-characterization of the used components, this approach might account better for experimental imperfections. Although the latter typically tend to reduce the degree of entanglement, our entanglement detection turns out to be quite robust against them.

Altogether, the method described above would, in principle, allow for a reconstruction of the output state as far as this is possible with four moments. We note that from such a reconstruction also all entanglement properties could be derived. However, as shown in the next section we choose a different approach.

C. Entanglement witness

The detection of entanglement requires substantially less information than a full state reconstruction. Indeed, there exists an infinite number of witnesses and criteria which allow one to decide whether or not a state is entangled. Each of these criteria uses only a small amount of information about the examined state. In this work, we use the witness matrix⁴⁸

$$\mathbf{M}^{(2)} \equiv \begin{pmatrix} 1 & \langle \hat{s}_1 \rangle & \langle \hat{s}_1^\dagger \rangle & \langle \hat{s}_2^\dagger \rangle & \langle \hat{s}_2 \rangle \\ \langle \hat{s}_1^\dagger \rangle & \langle \hat{s}_1^\dagger \hat{s}_1 \rangle & \langle (\hat{s}_1^\dagger)^2 \rangle & \langle \hat{s}_1^\dagger \hat{s}_2^\dagger \rangle & \langle \hat{s}_1^\dagger \hat{s}_2 \rangle \\ \langle \hat{s}_1 \rangle & \langle \hat{s}_1 \rangle & 1 + \langle \hat{s}_1^\dagger \hat{s}_1 \rangle & \langle \hat{s}_1 \hat{s}_2^\dagger \rangle & \langle \hat{s}_1 \hat{s}_2 \rangle \\ \langle \hat{s}_2 \rangle & \langle \hat{s}_1 \hat{s}_2 \rangle & \langle \hat{s}_1^\dagger \hat{s}_2 \rangle & \langle \hat{s}_2^\dagger \hat{s}_2 \rangle & \langle \hat{s}_2 \rangle \\ \langle \hat{s}_2^\dagger \rangle & \langle \hat{s}_1 \hat{s}_2^\dagger \rangle & \langle \hat{s}_1^\dagger \hat{s}_2^\dagger \rangle & \langle (\hat{s}_2^\dagger)^2 \rangle & 1 + \langle \hat{s}_2^\dagger \hat{s}_2 \rangle \end{pmatrix}, \quad (24)$$

which contains up to second order moments of the beam splitter output state. If $\mathbf{M}^{(2)}$ has at least one negative eigenvalue, the state is entangled. The absence of a negative eigenvalue implies separability only in the case of Gaussian states.

D. Negativity

For a bipartite system, the amount of entanglement between the subsystems A and B can be quantified by means of the negativity

$$\mathcal{N}(\rho) \equiv \frac{\|\rho^{TB}\|_1 - 1}{2}, \quad (25)$$

where ρ is the density matrix of the total system, and $\|\rho^{TB}\|_1 = \text{Tr}|\rho^{TB}|$ is the trace norm of the partial transpose of ρ with respect to subsystem B, ρ^{TB} . If $\mathcal{N}(\rho) > 0$, the state is entangled. For a maximally entangled state, $\mathcal{N}(\rho) \rightarrow \infty$.

In the case of Gaussian states, all measures of entanglement are equivalent, and they are defined by the covariance matrix

$$\sigma = \begin{pmatrix} \boldsymbol{\alpha} & \boldsymbol{\gamma} \\ \boldsymbol{\gamma}^T & \boldsymbol{\beta} \end{pmatrix}. \quad (26)$$

Here, we define the matrices

$$\boldsymbol{\alpha} \equiv \begin{pmatrix} \alpha_1 & \alpha_3 \\ \alpha_3 & \alpha_2 \end{pmatrix}, \boldsymbol{\beta} \equiv \begin{pmatrix} \beta_1 & \beta_3 \\ \beta_3 & \beta_2 \end{pmatrix}, \boldsymbol{\gamma} \equiv \begin{pmatrix} \gamma_{11} & \gamma_{12} \\ \gamma_{21} & \gamma_{22} \end{pmatrix} \quad (27)$$

with

$$\alpha_1 = \langle \hat{s}_1^2 \rangle + \langle (\hat{s}_1^\dagger)^2 \rangle + 2\langle \hat{s}_1^\dagger \hat{s}_1 \rangle - \langle \hat{s}_1 + \hat{s}_1^\dagger \rangle^2 + 1 \quad (28)$$

$$\alpha_2 = -\langle \hat{s}_2^2 \rangle - \langle (\hat{s}_2^\dagger)^2 \rangle + 2\langle \hat{s}_2^\dagger \hat{s}_2 \rangle + \langle \hat{s}_2 - \hat{s}_2^\dagger \rangle^2 + 1 \quad (29)$$

$$\alpha_3 = i(-\langle \hat{s}_1^2 \rangle + \langle (\hat{s}_1^\dagger)^2 \rangle + \langle \hat{s}_1 \rangle - \langle \hat{s}_1^\dagger \rangle^2) \quad (30)$$

$$\beta_1 = \langle \hat{s}_2^2 \rangle + \langle (\hat{s}_2^\dagger)^2 \rangle + 2\langle \hat{s}_2^\dagger \hat{s}_2 \rangle - \langle \hat{s}_2 + \hat{s}_2^\dagger \rangle^2 + 1 \quad (31)$$

$$\beta_2 = -\langle \hat{s}_2^2 \rangle - \langle (\hat{s}_2^\dagger)^2 \rangle + 2\langle \hat{s}_2^\dagger \hat{s}_2 \rangle + \langle \hat{s}_2 - \hat{s}_2^\dagger \rangle^2 + 1 \quad (32)$$

$$\beta_3 = i(-\langle \hat{s}_2^2 \rangle + \langle (\hat{s}_2^\dagger)^2 \rangle + \langle \hat{s}_2 \rangle^2 - \langle \hat{s}_2^\dagger \rangle^2) \quad (33)$$

$$\begin{aligned} \gamma_{11} = & \langle \hat{s}_1 \hat{s}_2 + \hat{s}_1 \hat{s}_2^\dagger + \hat{s}_1^\dagger \hat{s}_2 + \hat{s}_1^\dagger \hat{s}_2^\dagger \rangle / 2 \\ & + \langle \hat{s}_2 \hat{s}_1 + \hat{s}_2 \hat{s}_1^\dagger + \hat{s}_2^\dagger \hat{s}_1 + \hat{s}_2^\dagger \hat{s}_1^\dagger \rangle / 2 \\ & - \langle \hat{s}_1 + \hat{s}_1^\dagger \rangle \langle \hat{s}_2 + \hat{s}_2^\dagger \rangle \end{aligned} \quad (34)$$

$$\begin{aligned} \gamma_{12} = & \langle \hat{s}_1 \hat{s}_2 - \hat{s}_1 \hat{s}_2^\dagger + \hat{s}_1^\dagger \hat{s}_2 - \hat{s}_1^\dagger \hat{s}_2^\dagger \rangle / 2i \\ & + \langle \hat{s}_2 \hat{s}_1 + \hat{s}_2 \hat{s}_1^\dagger - \hat{s}_2^\dagger \hat{s}_1 - \hat{s}_2^\dagger \hat{s}_1^\dagger \rangle / 2i \\ & + i\langle \hat{s}_1 + \hat{s}_1^\dagger \rangle \langle \hat{s}_2 - \hat{s}_2^\dagger \rangle \end{aligned} \quad (35)$$

$$\begin{aligned} \gamma_{21} = & \langle \hat{s}_1 \hat{s}_2 + \hat{s}_1 \hat{s}_2^\dagger - \hat{s}_1^\dagger \hat{s}_2 - \hat{s}_1^\dagger \hat{s}_2^\dagger \rangle / 2i \\ & + \langle \hat{s}_2 \hat{s}_1 - \hat{s}_2 \hat{s}_1^\dagger + \hat{s}_2^\dagger \hat{s}_1 - \hat{s}_2^\dagger \hat{s}_1^\dagger \rangle / 2i \\ & + i\langle \hat{s}_1 - \hat{s}_1^\dagger \rangle \langle \hat{s}_2 + \hat{s}_2^\dagger \rangle \end{aligned} \quad (36)$$

$$\begin{aligned} \gamma_{22} = & \langle -\hat{s}_1 \hat{s}_2 + \hat{s}_1 \hat{s}_2^\dagger + \hat{s}_1^\dagger \hat{s}_2 - \hat{s}_1^\dagger \hat{s}_2^\dagger \rangle / 2 \\ & + \langle -\hat{s}_2 \hat{s}_1 + \hat{s}_2 \hat{s}_1^\dagger + \hat{s}_2^\dagger \hat{s}_1 - \hat{s}_2^\dagger \hat{s}_1^\dagger \rangle / 2 \\ & + \langle \hat{s}_1 - \hat{s}_1^\dagger \rangle \langle \hat{s}_2 - \hat{s}_2^\dagger \rangle \end{aligned} \quad (37)$$

and γ^T being the transpose of γ . Finally, the negativity becomes⁴⁹

$$\mathcal{N} = \max \left\{ 0, \frac{1 - \nu}{2\nu} \right\} \equiv \max \left\{ 0, \tilde{\mathcal{N}} \right\}, \quad (38)$$

where $\nu \equiv \sqrt{(\Delta(\boldsymbol{\sigma}) - \sqrt{\Delta^2(\boldsymbol{\sigma}) - 4 \det \boldsymbol{\sigma}}) / 2}$ and $\Delta(\boldsymbol{\sigma}) \equiv \det \boldsymbol{\alpha} + \det \boldsymbol{\beta} - 2 \det \boldsymbol{\gamma}$.

Note that, despite not being a measure, the negativity kernel $\tilde{\mathcal{N}}$ is a witness for arbitrary bipartite entanglement. In fact, if a non-Gaussian state has the same first and second moments as an entangled Gaussian state, it is entangled⁵⁰. Consequently, $\tilde{\mathcal{N}} > 0$ implies entanglement for any bipartite state.

E. Verifying consistency with a Gaussian state using higher order cumulants

In order to check whether the states we reconstruct are consistent with Gaussian states, we evaluate the $(l+m)$ th order cumulants $\langle\langle (\hat{a}^l)^\dagger \hat{a}^m \rangle\rangle$ for $l+m \leq 4$ and $l, m \in \mathbb{N}_0$. Equivalently to the moments, the cumulants describe a probability distribution. The definition of cumulant for a quantum state with density matrix ρ can be written as⁵¹

$$\langle\langle (\hat{a}^l)^\dagger \hat{a}^m \rangle\rangle \equiv \frac{\partial^l}{\partial (i\beta^*)^l} \frac{\partial^m}{\partial (i\beta)^m} \left[\frac{\beta\beta^*}{2} + \ln \text{Tr} \left(e^{(i\beta^* \hat{a}^\dagger + i\beta \hat{a})} \rho \right) \right]_{\beta, \beta^* = 0}. \quad (39)$$

Only Gaussian states have a finite number of nonzero cumulants. More specifically, all their cumulants vanish for $l+m > 2$. In other words, finding a nonzero cumulant of 3rd or higher order implies that the state is not Gaussian. Despite not being a strict proof, the fact that the 3rd and 4th order cumulant are very small or vanish in an experimental reconstruction constitutes a reasonable indication that the reconstructed state is Gaussian.

As an example we spell out the 3rd order cumulants as functions of the moments at the beam splitter outputs reconstructed with the reference-state method. We find⁵²

$$\langle\langle \hat{s}_{1,2}^3 \rangle\rangle = \langle \hat{s}_{1,2}^3 \rangle - 3\langle \hat{s}_{1,2}^2 \rangle \langle \hat{s}_{1,2} \rangle + 2\langle \hat{s}_{1,2} \rangle^3 \quad (40)$$

$$\begin{aligned} \langle\langle \hat{s}_{1,2}^\dagger \hat{s}_{1,2}^2 \rangle\rangle = & \langle \hat{s}_{1,2}^\dagger \hat{s}_{1,2}^2 \rangle - \langle \hat{s}_{1,2}^\dagger \rangle \langle \hat{s}_{1,2}^2 \rangle \\ & - 2\langle \hat{s}_{1,2}^\dagger \hat{s}_{1,2} \rangle \langle \hat{s}_{1,2} \rangle + 2\langle \hat{s}_{1,2}^\dagger \rangle \langle \hat{s}_{1,2} \rangle^2. \end{aligned} \quad (41)$$

ACKNOWLEDGMENTS

The authors thank Christopher Eichler for discussions. We acknowledge support from the Deutsche Forschungsgemeinschaft via the Sonderforschungsbereich 631, the German excellence initiative via the ‘Nanosystems Initiative Munich’ (NIM), from the EU projects SOLID, CC-QED and PROMISCE, from MEXT Kakenhi ‘Quantum Cybernetics’, the JSPS through its FIRST Program, the Project for Developing Innovation Systems of MEXT, the NICT Commissioned Research, EPSRC EP/H050434/1, Basque Government IT472-10, and Spanish MICINN FIS2009-12773-C02-01.

* Edwin.Menzel@wmi.badw-muenchen.de

³¹ T. Yamamoto, K. Inomata, M. Watanabe, K. Matsuba, T. Miyazaki, W. D. Oliver, Y. Nakamura, and J. S. Tsai, *Appl. Phys. Lett.* **93**, 042510 (2008).

³² R. E. Collin, *Foundations for Microwave Engineering*, 2nd ed. (Wiley and Sons, New York, 2001).

³³ M. Mariani, E. P. Menzel, F. Deppe, M. Á. Araque-Caballero, A. Baust, T. Niemczyk, E. Hoffmann, E. Solano,

A. Marx, and R. Gross, *Phys. Rev. Lett.* **105**, 133601 (2010).

³⁴ E. Hoffmann, F. Deppe, T. Niemczyk, T. Wirth, E. P. Menzel, G. Wild, H. Huebl, M. Mariani, T. Weißl, A. Lukashenko, A. P. Zhuravel, A. V. Ustinov, A. Marx, and R. Gross, *Appl. Phys. Lett.* **97**, 222508 (2010).

³⁵ Z. Y. Ou, S. F. Pereira, H. J. Kimble, and K. C. Peng, *Phys. Rev. Lett.* **68**, 3663 (1992).

- ³⁶ U. Leonhardt, *Measuring the Quantum State of Light* (Cambridge University Press, Cambridge, 1997).
- ³⁷ B. Peropadre, G. Romero, G. Johansson, C. M. Wilson, E. Solano, and J. J. García-Ripoll, *Phys. Rev. A* **84**, 063834 (2011).
- ³⁸ Y.-F. Chen, D. Hover, S. Sendelbach, L. Maurer, S. T. Merkel, E. J. Pritchett, F. K. Wilhelm, and R. McDermott, *Phys. Rev. Lett.* **107**, 217401 (2011).
- ³⁹ A. Poudel, R. McDermott, and M. G. Vavilov, arXiv:1201.2990v1 (2012).
- ⁴⁰ E. P. Menzel, F. Deppe, M. Mariani, M. Á. Araque Caballero, A. Baust, T. Niemczyk, E. Hoffmann, A. Marx, E. Solano, and R. Gross, *Phys. Rev. Lett.* **105**, 100401 (2010).
- ⁴¹ D. Bozyigit, C. Lang, L. Steffen, J. M. Fink, C. Eichler, M. Baur, R. Bianchetti, P. J. Leek, S. Filipp, M. P. da Silva, A. Blais, and A. Wallraff, *Nature Phys.* **7**, 154 (2011).
- ⁴² C. Eichler, D. Bozyigit, C. Lang, L. Steffen, J. Fink, and A. Wallraff, *Phys. Rev. Lett.* **106**, 220503 (2011).
- ⁴³ C. Eichler, D. Bozyigit, C. Lang, M. Baur, L. Steffen, J. M. Fink, S. Filipp, and A. Wallraff, *Phys. Rev. Lett.* **107**, 113601 (2011).
- ⁴⁴ M. P. da Silva, D. Bozyigit, A. Wallraff, and A. Blais, *Phys. Rev. A* **82**, 043804 (2010).
- ⁴⁵ C. M. Caves, *Phys. Rev. D* **26**, 1817 (1982).
- ⁴⁶ V. Bužek, G. Adam, and G. Drobný, *Phys. Rev. A* **54**, 804 (1996).
- ⁴⁷ V. Bužek, G. Adam, and G. Drobný, *Ann. Phys.* **245**, 37 (1996).
- ⁴⁸ E. Shchukin and W. Vogel, *Phys. Rev. Lett.* **95**, 230502 (2005).
- ⁴⁹ G. Adesso and F. Illuminati, *Phys. Rev. A* **72**, 032334 (2005).
- ⁵⁰ P. Hyllus and J. Eisert, *New J. Phys.* **8**, 51 (2006).
- ⁵¹ R. Schack and A. Schenzle, *Phys. Rev. A* **41**, 3847 (1990).
- ⁵² L.-Z. Jiang, *Proc. of SPIE* **7846**, 784612 (2010).